Radio Galaxy Zoo: observational evidence for environment as the cause of radio source asymmetry

P. E. Rodman [ID],[1]★ R. J. Turner,[1,2] S. S. Shabala [ID],[1] J. K. Banfield [ID],[3] O. I. Wong [ID],[4,5]
H. Andernach,[6] A. F. Garon [ID],[7] A. D. Kapińska,[8] R. P. Norris, [ID][9] and L. Rudnick [ID][7]

[1]*School of Natural Sciences, Private Bag 37, University of Tasmania, Hobart, TAS 7001, Australia*
[2]*CSIRO Australia Telescope National Facility, PO Box 76, Epping, NSW 1710, Australia*
[3]*Research School of Astronomy and Astrophysics, Australian National University, Canberra ACT, 2611, Australia*
[4]*International Centre for Radio Astronomy Research-M468, The University of Western Australia, 35 Stirling Hwy, Crawley, WA 6009, Australia*
[5]*ARC Centre of Excellence for All-sky Astrophysics (CAASTRO), Building A28, School of Physics, The University of Sydney, NSW 2006, Australia*
[6]*Departamento de Astronomía, DCNE, Universidad de Guanajuato, Apdo. Postal 144, CP 36000, Guanajuato, Gto., Mexico*
[7]*Minnesota Institute for Astrophysics, University of Minnesota, 116 Church St. SE, Minneapolis, MN 55455, USA*
[8]*National Radio Astronomy Observatory (NRAO), 1003 Lopezville Road, Socorro, NM 87801-0387, USA*
[9]*Western Sydney University, Locked Bag 1797, Penrith, NSW 2751, Australia*

ABSTRACT

We investigate the role of environment on radio galaxy properties by constructing a sample of large ($\gtrsim 100$ kpc), nearby ($z < 0.3$) radio sources identified as part of the Radio Galaxy Zoo citizen science project. Our sample consists of 16 Fanaroff-Riley Type II (FR-II) sources, 6 FR-I sources, and 1 source with a hybrid morphology. FR-I sources appear to be hosted by more massive galaxies, consistent with previous studies. In the FR-II sample, we compare the degree of asymmetry in radio lobe properties to asymmetry in the radio source environment, quantified through optical galaxy clustering. We find that the length of radio lobes in FR-II sources is anticorrelated with both galaxy clustering and lobe luminosity. These results are in quantitative agreement with predictions from radio source dynamical models and suggest that galaxy clustering provides a useful proxy for the ambient gas density distribution encountered by the radio lobes.

Key words: galaxies: active – galaxies: jets – radio continuum: galaxies.

1 INTRODUCTION

In the local Universe, radio-loud active galactic nuclei (AGN) are predominantly hosted by massive elliptical galaxies (Sadler, Jenkins & Kotanyi 1989; Burns 1990). Optical properties of host galaxies of these AGN show a striking dichotomy: radio AGN with strong emission lines (so-called high-excitation radio galaxies, or HERGs) are hosted by lower mass galaxies than low-excitation radio galaxies (LERGs; Best & Heckman 2012). The radio AGN fraction in LERGs shows a strong mass dependence (Best et al. 2005), with massive galaxies more likely to host an AGN. Even at fixed stellar mass, brightest cluster galaxies host a higher fraction of radio AGN (Best et al. 2007). Dynamical state of the cluster is also important, with almost all rapidly cooling clusters hosting radio AGN, compared to fewer than half for clusters with cooling times in excess of 1 Gyr (Mittal et al. 2009). These findings can be explained in a framework where LERGs are triggered by gradual cooling of the gas out of the hot halo (Hardcastle, Evans & Croston 2007),

a fraction of this gas being eventually accreted by the black hole, possibly via chaotic cold accretion (Gaspari, Brighenti & Temi 2015). Models in which LERGs operate as thermostats are quantitatively consistent with the observed scaling of the radio AGN duty cycle with mass (Shabala et al. 2008; Pope, Mendel & Shabala 2012). Conversely, the fraction of high-excitation radio AGN is enhanced in the presence of one-on-one interactions between galaxies (Sabater, Best & Argudo-Fernández 2013; Ellison, Patton & Hickox 2015), and their host galaxies often show disturbed morphologies and high dust masses (Kaviraj et al. 2012; Shabala, Santoso & Godfrey 2012; Tadhunter et al. 2014), consistent with being triggered through galaxy interactions.

Once a jet is triggered, environment plays an important role in determining the final lobe morphology. At low redshift, edge-darkened, or Fanaroff-Riley (FR; Fanaroff & Riley 1974) Type I, objects are mostly found in clusters, while edge-brightened, or FR-II, sources prefer poorer environments (Hill & Lilly 1991). FR-IIs have higher radio luminosities than FR-Is, and the two FR classes show a difference in characteristic radio luminosity which increases with host galaxy optical luminosity (Owen & Ledlow 1994); how-

★ E-mail: payton.rodman@utas.edu.au

ever, both FR classes show a large scatter and overlap in radio luminosity (Best 2009; Miraghaei & Best 2017). This morphological distinction is an important factor in the radio source–environment interaction: while FR-Is provide gentle, quasi-continuous heating to cluster cores (e.g. Churazov et al. 2001; Fabian 2012), FR-IIs drive powerful shocks capable of affecting satellite galaxies on scales of hundreds of kiloparsecs (Rawlings & Jarvis 2004; Shabala, Kaviraj & Silk 2011). There is a loose association between FR morphology and optical classification, in the sense that almost all FR-Is are LERGs, but FR-IIs can be hosted by both high and (less often) low-excitation galaxies. A growing consensus appears to be that the FR classification may be determined by jet–environment interaction on approximately kiloparsec scales: if the initially relativistic jet can be slowed down sufficiently via entrainment from the interstellar medium (Bicknell 1995) or stellar winds (Komissarov 1994; Perucho et al. 2014), it will eventually be disrupted and form a FR-I; on the other hand, if the jet is not entrained appreciably, it will form a characteristic FR-II structure with lobes inflated via backflow of overpressured plasma from jet termination shocks, seen in radio images as hotspots. Alternatives to jet entrainment are jet stalling in a rising pressure profile (Massaglia et al. 2016), or failed collimation of an initially conical jet by the environment (Alexander 2006; Krause et al. 2012); both are followed by eventual jet disruption and transition to an FR-I as a result of jet–environment interaction. A small fraction (less than 1 per cent; Gawroński et al. 2006) of extended radio sources show hybrid morphologies (Gopal-Krishna & Wiita 2000; Kapińska et al. 2017), with FR-I morphology on one side of the central engine, and FR-II morphology of the other. These objects are ideal laboratories for studying the interaction of the small-scale jets with their environment: the two jets are intrinsically identical, and the difference in the final morphology can be attributed to different kinds of interaction with the environment.

On larger scales (tens and hundreds of kpc), environment is a key factor in lobe (rather than jet) evolution. Dynamical radio source models (e.g. Kaiser & Alexander 1997; Blundell & Rawlings 2000; Turner & Shabala 2015; Hardcastle 2018) and numerical simulations (Hardcastle & Krause 2013, 2014) predict that the temporal evolution of lobe size and luminosity should be strongly environment dependent; these predictions are consistent with X-ray observations (Arnaud et al. 2010). Compact radio AGN are more prevalent in low-mass galaxies and poor environments (Shabala 2018), consistent with models in which extended emission may be below the surface brightness detection threshold of existing instruments (Shabala et al. 2017; Turner, Shabala & Krause 2018b); recent increased sensitivity observations of giant lobes in the archetypal FR-I source 3C31 (Heesen et al. 2018) confirms this picture. Estimates of AGN lifetimes and jet kinetic powers from radio continuum data are therefore environment dependent, and hence so too are estimates of the energy budget available for AGN feedback; this feedback process is responsible for shaping the bright end of the galaxy luminosity function (Silk & Rees 1998; Bower et al. 2006; Croton et al. 2006). Environment quantification through galaxy clustering provides a natural connection between galaxy formation and lobe evolution models. Turner & Shabala (2015) used a semi-analytic galaxy formation model to quantify radio source environments and showed that this approach can explain many properties of the observed radio galaxy populations. Shabala & Alexander (2009) and Raouf et al. (2017) modelled radio AGN and galaxy properties self-consistently within a semi-analytic galaxy formation model and showed that the requirement to match radio AGN and galaxy properties simultaneously places powerful constraints on feedback models.

In this paper, we present an analysis of a sample of Radio Galaxy Zoo (hereafter RGZ; Banfield et al. 2015) radio galaxies with large-scale environment information from galaxy clustering. The focus of the paper is on exploring the relationship between the asymmetry in radio lobe properties, and asymmetry in radio source environments quantified through galaxy clustering. We present our sample in Sections 2 and 3, and discuss the role of environment on lobe evolution in Section 4. We conclude in Section 5.

Throughout the paper, we assume a flat Universe with $H_0 = 68 \, \mathrm{km \, s^{-1} \, Mpc^{-1}}$, $\Omega_\Lambda = 0.685$ and $\Omega_M = 0.315$ (Planck Collaboration XVI 2014).

2 SAMPLE SELECTION

The starting point for our sample is the set of multicomponent radio sources identified by citizen scientists through the RGZ project (Banfield et al. 2015). RGZ enlists citizen scientists to classify 1.4 GHz radio continuum images from the Faint Images of the Radio Sky at Twenty Centimeters (FIRST; Becker, White & Helfand 1995) and the Australian Telescope Large Area Survey (ATLAS; Norris et al. 2006; Middelberg et al. 2008) projects. RGZ offers to its volunteers a superposition of these radio images with mid-infrared images at $3.4 \, \mu m$ from the *Wide-field Infrared Survey Explorer* (*WISE*; Wright et al. 2010) and at $3.6 \, \mu m$ from the *Spitzer* Wide-Area Infrared Extragalactic Survey (SWIRE; Lonsdale et al. 2003). Citizen scientists are asked to identify whether separate radio source components may belong to a single radio structure, and whether there is a corresponding infra-red host galaxy. Upon achieving a sufficient number of classifications for one image (20 for non-compact sources), the consensus level C is evaluated for the radio and infra-red classifications of each source. The consensus on the position of the host galaxy is then determined through application of a kernel-density estimator (KDE) on the positions clicked by the volunteers since these positions may differ by a few pixels and yet be identifying the same source. We refer the interested reader to Banfield et al. (2015) for further details.

The initial data set contained 2679 candidate sources with two or three radio components from the subset of the RGZ catalogue investigated by Banfield et al. (2015). The sample was reduced to those sources with a consensus level above 0.7 and redshift $z < 0.3$, reducing the sample to 169 sources. Radio lobes were required to be approximately straight to allow for accurate quantification of lobe length and environment (within ~10 deg; see below), reducing the sample to 89. We required at least one of the radio lobes to be at least 100 kpc in length as measured along a straight line from the host to the emission region farthest from the host, to ensure sufficient image resolution. Finally, an integrated flux density threshold of 20 mJy was imposed to ensure sufficiently high signal-to-noise ratio.

In this work, we seek to probe the relationship between radio source morphology and environment; this is achieved using the Sloan Digital Sky Survey (SDSS) DR10 (Ahn et al. 2014) and the photometric redshifts of Beck et al. (2016) to quantify galaxy clustering near our radio sources. To ensure robust quantification of the environment, neighbouring galaxies were associated to the host using photometric redshifts; galaxies with photometric redshifts consistent with the host spectroscopic or photometric redshift (within 3 sigma uncertainties) were admitted as neighbours. In addition, we required each source to have at least 20 such neighbour galaxies within a projected distance of 1 Mpc of the host galaxy.

The large tolerance in redshift is chosen to ensure that for host galaxies located in clusters, all cluster members are included; we note some nearby isolated galaxies may also be included, adding
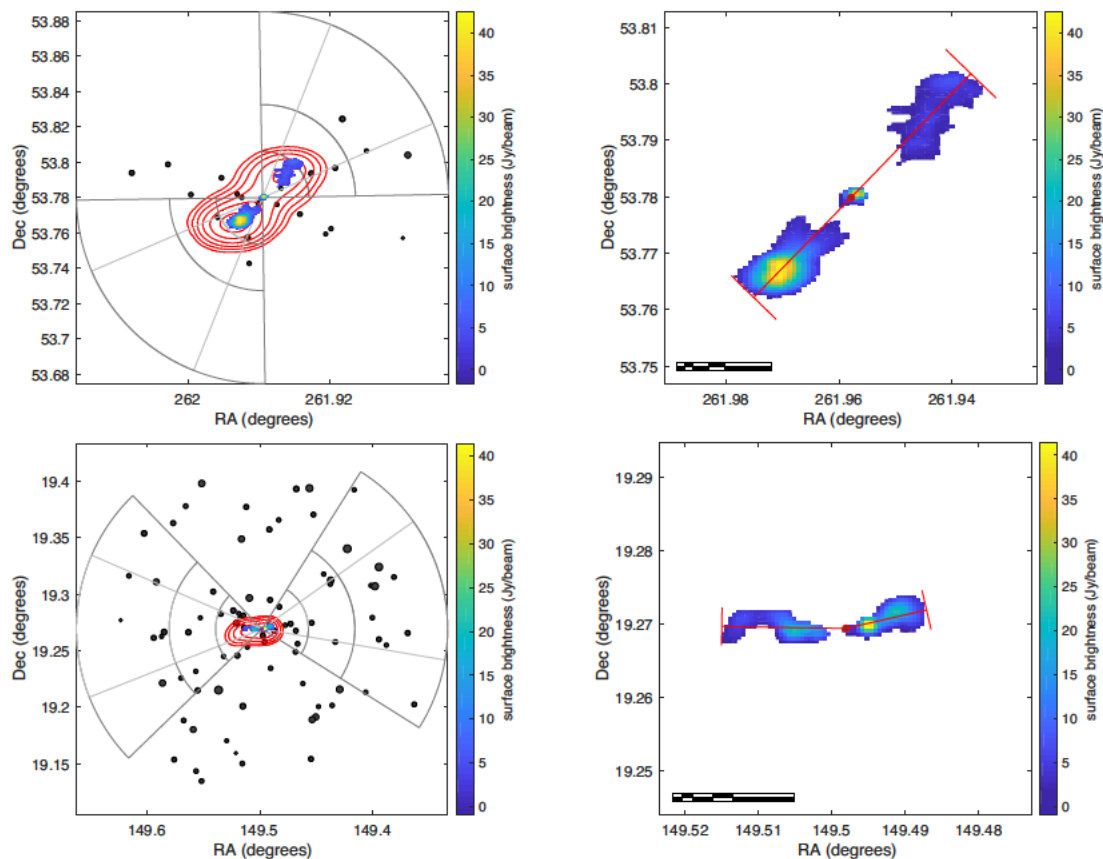
Figure 1. *Top left:* Radio-optical overlays for the FR-II source RGZ J172749.5 + 534647. Colour scale shows 1.4 GHz FIRST surface brightness, red contours are 1.4 GHz NVSS surface brightness at 5, 10, 20, 40, 80, and 160σ. Black circles are optical galaxies with redshifts consistent with the radio source host; symbol size is proportional to z-band magnitude of each galaxy. Wedges of 45 and 90 deg centred on the lobe axis are shown, with arcs drawn at 250, 500, and 1000 kpc from the AGN host. *Top right:* Zoom-in on the radio emission; the scale bar is 1 arcmin in length, and subdivided into units of 5, 10, 20, and 30 arcsec. Red lines are indicative of axis lengths and jet directions; cross-bars at the end are the width of the fitted box. *Bottom:* FR-I source RGZ J095759.3 + 191609; symbols are as above. Radio-optical overlays for the remaining FR-II and FR-I sources can be found in Appendix A and Appendix B, respectively.
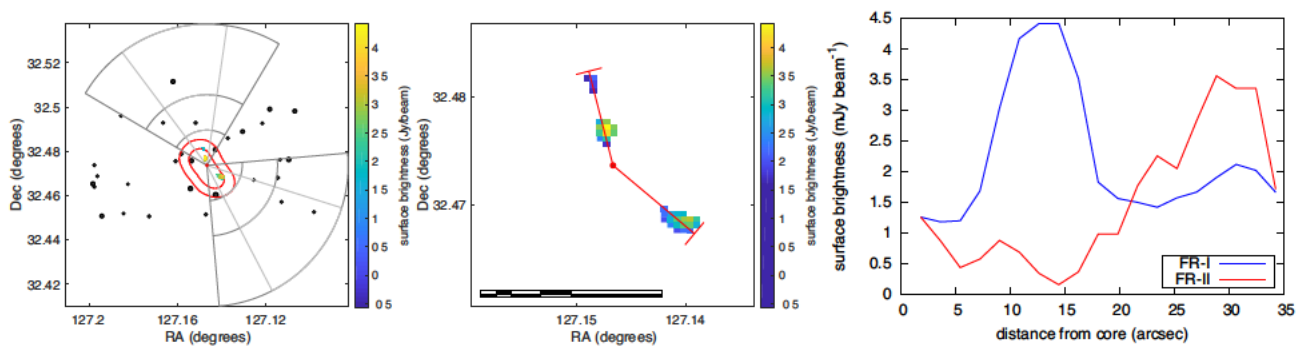
Figure 2. *Left and middle:* Hybrid source RGZ J082835.2 + 322825; symbols are as in Fig. 1. *Right:* The surface brightness profile along the lobe major axis of the hybrid source RGZ J082835.2 + 322825, measured from the active nucleus towards the extrema of each lobe. The profile of the eastern-most lobe (blue) is of characteristic FR-I type, whereas that of the western-most lobe (red) describes an FR-II.

noise to our measurements. Imposing more stringent requirements of 2σ or 1σ would reduce the number of neighbours by $\sim$17 per cent and $\sim$38 per cent, respectively. We repeated our analysis below using these more stringent cuts, and reproduced the same conclusions with lower statistical significance. The threshold galaxy counts requirement biases the sample against sources in poor environments, but makes our analysis more robust to outliers.

Our final sample consists of 23 extended RGZ sources seen in the FIRST survey at $z < 0.3$ with environment information. Radio and optical images of these sources and their surrounding environment
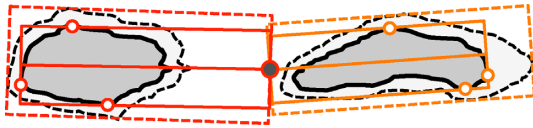
Figure 3. Definition of the spatial extent of the radio lobes using the outermost 5σ (solid rectangles) for an FR-II type lobe (*left*) and an FR-I type lobe (*right*). Associated 3σ contours (dashed rectangles) are used to estimate the uncertainty of the spatial extent. Bounding rectangles are chosen such that (i) the active nucleus lies at the mid-point on the base of the rectangle (filled circle), and (ii) the remaining sides are tangent to the extrema of the lobe (open circles). Radio lobes with lobe axes differing by more than approximately 10 deg, or whose axes are not confined within the horizontal extent of the lobe (i.e. are highly bent), are excluded from our analysis.
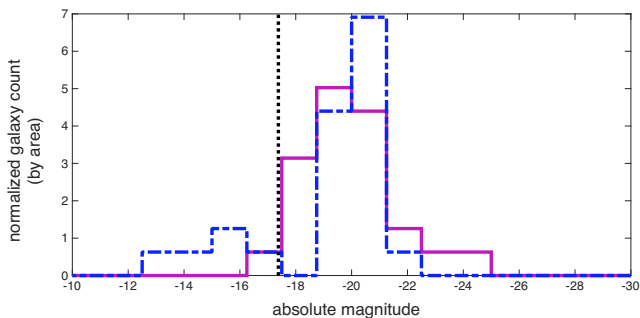
Figure 4. The distribution of absolute z-band magnitudes of galaxies surrounding FR-I source RGZ J095759.3 + 191609 (Fig. B3), normalized to the area of the containing 90 deg wedge. The solid line corresponds to the western-most lobe, and the dot-dashed line to the eastern-most lobe. The dotted line is the 95 per cent completeness limit on the absolute z-band magnitude. Normalized galaxy counts are lower for galaxies less luminous than this limit, as expected.

are presented in Appendices A and B, with one example of each class (FR-II, FR-I, and hybrid) shown in the main text.

3 RESULTS

The objective of this work is to investigate the relationship between asymmetries in radio source properties and those of its environment. Below, we briefly outline quantitative measures of asymmetry in radio source size, luminosity, and morphology (Section 3.1), as well as environment as described by galaxy clustering (Section 3.2).

3.1 Radio source properties

Following the approach of Fanaroff & Riley (1974), radio lobes were separated into Fanaroff-Riley Type I (edge-darkened) or Type II (edge-brightened) morphological classes; radio sources with lobes of different morphology (i.e. FR-I on one side of the central engine, FR-II on the other) are classified as hybrids. Visual classifications were performed by three of the authors (PER, RJT, SSS), resulting in a sample consisting of 16 FR-IIs, 6 FR-Is, and 1 hybrid. The northern lobe of one further source, RGZ J102733.6 + 481718, has a borderline FR-I/II morphology and could not be reliably classified; this source was excluded from further analysis. Examples of an FR-I and FR-II source in our sample are shown in Fig. 1; the one hybrid source is shown in Fig. 2. The remaining FR-II sources are presented in Appendix A, and the remaining FR-I sources in Appendix B. Relevant properties of all sources in our sample are given in Table 1.

We define the spatial extent of each source by the outermost 5σ contours ($\sigma \sim 0.15$ mJy beam^{-1}). Following Turner et al. (2018a), the source is divided into two radio lobes by finding the two most extreme points and associating the other pixels of emission to the extreme point on the same side of the host optical galaxy. A rectangular box is then fitted to each lobe so that it intersects the extreme point and has the host optical galaxy bisect the opposite edge; the box is rotated so that the two edges parallel to the lobe major axis are tangent to the 5σ contour (see Fig. 3). The length of each lobe is then taken to be the length of this rectangular box outwards from the central engine, and the flux density as the integrated surface brightness. The uncertainty in these parameters is quantified by comparing these estimates to those fitted assuming a lower 3σ contour. For FR-II sources, the lobe length thus defined typically corresponds to the distance between the core and edge of the lobe. For FR-Is, lobe length defined in this way will necessarily be sensitivity limited (e.g. Turner et al. 2018a); however, this does not bias our results as we are interested in the ratio of the lobe lengths of individual sources.

We use the location of the brightest point in each lobe to calculate the Fanaroff-Riley index, $FR = 2x_{bright}/x_{length} + 1/2$; in this formulation FR-Is have indices $0.5 < FR < 1.5$ and FR-IIs have $1.5 < FR < 2.5$ (Krause et al. 2012). The numerical values obtained are in excellent agreement with visual classifications. As shown in Table 1, all visually identified FR-II lobes have FR indices well in excess of 1.5, with the exception of the southern lobe of RGZ J093821.5+554333, where the small lobe size and source curvature are likely to render lobe length measurement unreliable. For FR-Is, only the eastern lobe of RGZ J094443.2+024754 has an FR index marginally in excess of 1.5; it also has an unusual double-knot structure in the jet. We note that our approach of measuring lobe lengths is an approximation, and cannot deal with curved sources. Below, we restrict our analysis to straight, FR-II sources for which our methodology is valid. There is one hybrid source, RGZ J082835.2 + 322825 (Fig. 2), with a clear FR-I morphology in the eastern lobe, and FR-II morphology in the western lobe. The source J125721.9 + 122820 shows diffuse emission almost perpendicular to the current lobe axis; such radio morphology could come about due to backflow in highly non-axysymmetric environments (Hodges-Kluck & Reynolds 2011), or be due to a previous jet episode (e.g. Chon et al. 2012). For the purposes of the present analysis we note that the morphology of the bright FR-II lobes is well-defined, and we therefore retain this source in our sample.

Finally, the lobe luminosities of some of the FR-IIs in our sample may be contaminated by hotspot emission (as seen in Figs A1–A15), which is unaccounted for in analytical radio source models. Hotspots are typically $\lesssim 1$ per cent of source size (Hardcastle et al. 1998; Godfrey & Shabala 2013), and hence sources with total length shorter than ~ 200 arcsec are likely to contain both lobe and hotspot emission at the peak brightness location. In Table 1, we quote the fraction of the total lobe flux density contained in hotspots. The integrated flux density in the eastern lobe of RGZ J210030.5 + 100529 (Fig. A15) arises almost entirely from unresolved (hotspot) emission, whereas 41 per cent of the emission in the western lobe is attributed to the hotspot. We conclude that this source has substantial hotspot contamination, and exclude it from the analysis.

3.2 Galaxy clustering

In quantifying galaxy clustering associated with each lobe, we consider galaxies within a 1 Mpc radius and with redshifts consistent within 3σ of the AGN host. The rectangular boxes fitted to the

Table 1. The samples of FR-IIs, hybrids, and FR-Is. Columns are: (1) source name; (2) redshift; (3) luminosity distance; (4) z-band absolute magnitude; (5) number of galaxies within 1 Mpc above $m_z = 20.5$ mag; (6) distance to fifth nearest neighbour; and (7) distance to 10th nearest neighbour. For the eastern / western radio lobes the columns are: (8/18, 9/19) lobe lengths for 5σ and 3σ cuts, respectively, measured along the jet axis; (10/20, 11/21) 1.4 GHz flux density from FIRST at the 5σ and 3σ cuts; (12/22) fraction of flux density in the hotspot; (13/23) Fanaroff-Riley morphology; (14/24, 15/25) number of galaxies within 500 kpc of the host and 45 or 90 deg of the lobe axis; and (16/26, 17/27) same as the previous columns but for 1 Mpc.

				Galaxy and cluster environment			Eastern lobe										Western lobe									
RGZ name	z	d_L	M_r	$N_{1\,\mathrm{Mpc}}$	d_5	d_{10}	D (kpc)		$S_{1.4}$ (mJy)		Hotspot	FR	$N_{500\,\mathrm{kpc}}$		$N_{1\,\mathrm{Mpc}}$		D (kpc)		$S_{1.4}$ (mJy)		Hotspot	FR	$N_{500\,\mathrm{kpc}}$		$N_{1\,\mathrm{Mpc}}$	
		(Mpc)		$(m_z>20.5)$	(kpc)	(kpc)	5σ	3σ	5σ	3σ	fraction		$45°$	$90°$	$45°$	$90°$	5σ	3σ	5σ	3σ	fraction		$45°$	$90°$	$45°$	$90°$
(1)	(2)	(3)	(4)	(5)	(6)	(7)	(8)	(9)	(10)	(11)	(12)	(13)	(14)	(15)	(16)	(17)	(18)	(19)	(20)	(21)	(22)	(23)	(24)	(25)	(26)	(27)
FR-IIs																										
RGZ J090542.6 + 465809	0.195[b]	979	−21.19	16	446	1023	141	142	76.4	83.1	0.23	2.17	0	2	1	6	187	189	60.3	67.7	0.30	2.31	1	3	1	5
RGZ J091445.5 + 413714	0.140	680	−23.86	14	154	240	133	137	202.0	205.2	0.13	1.98	1	3	4	8	106	106	164.0	167.3	0.16	2.09	6	8	10	14
RGZ J093821.5 + 554333	0.221	1126	−22.53	26	187	370	91	114	26.7	28.4	0.19	1.58	3	8	5	12	148	156	19.3	21.8	0.14	2.01	0	1	3	6
RGZ J100128.8 + 043437	0.222	1131	−23.29	37	351	484	192	197	27.6	30.0	0.19	2.11	1	9	2	12	147	150	34.7	37.7	0.22	2.15	3	8	6	15
RGZ J102040.8 + 315509	0.286	1508	−23.15	17	213	441	138	145	13.1	17.3	0.18	2.15	0	4	0	5	175	181	17.2	19.9	0.17	2.17	2	4	2	4
RGZ J110253.0 + 125904	0.140	680	−22.94	17	219	444	211	216	11.9	17.3	0.19	2.41	0	1	5	9	243	252	7.2	13.4	0.27	2.42	1	2	4	11
RGZ J120118.2 + 124500	0.278[b]	1460	−22.22	18	295	444	112	114	134.0	136.4	0.09	1.75	3	7	4	8	167	170	85.5	89.0	0.08	2.09	1	1	2	2
RGZ J125721.9 + 122820	0.208	1052	−22.43	13	196	431	119	123	84.0	90.1	0.11	2.13	0	1	0	8	131	136	170.0	176.4	0.31	2.17	0	1	1	5
RGZ J125724.2 + 063114	0.175	868	−21.91	12	480	586	123	126	19.9	25.8	0.18	1.80	1	3	7	10	175	179	9.1	16.5	0.29	2.02	2	4	2	6
RGZ J135110.8 + 072846	0.150	733	−22.67	9	270	380	151	152	105.0	115.0	0.23	1.98	3	6	3	6	130	135	89.7	97.5	0.24	2.15	5	6	5	9
RGZ J153008.0 + 231616	0.090	423	−23.29	31	393	732	265	272	50.4	62.4	0.10	2.25	5	10	5	12	265	271	55.7	64.1	0.09	2.07	5	7	5	10
RGZ J154936.7 + 361417	0.236	1212	−23.01	14	334	597	72	78	5.2	8.5	0.29	2.25	2	4	2	4	71	72	9.41	14.5	0.21	2.27	1	4	1	4
RGZ J161037.5 + 060509	0.241	1241	−22.45	13	506	603	177	189	18.1	23.9	0.16	2.08	1	4	2	7	158	176	17.9	23.0	0.15	2.13	2	2	3	5
RGZ J172749.5 + 534647	0.244[b]	1259	−22.17	21	165	321	191	193	470.0	486.7	0.05	1.93	3	5	3	5	237	239	166.0	188.2	0.03	2.24	3	3	5	6
RGZ J172957.2 + 450623	0.255[b]	1323	−22.29	12	490	663	299	305	142.0	155.8	0.08	2.20	2	3	2	3	281	291	127.0	142.3	0.08	2.23	6	7	6	7
RGZ J210030.5 + 100529[a]	0.156[b]	765	−22.46	12	294	466	125	175	1.2	12.7	∼1	2.32	0	1	0	1	160	169	10.8	18.7	0.44	2.16	1	2	5	7
Hybrids																										
RGZ J082835.2 + 322825	0.280	1472	−22.93	19	446	1023	140	149	7.7	12.7	0.48	1.25	1	3	2	4	139	144	7.6	10.0	0.40	2.24	2	7	2	7
FR-Is																										
RGZ J085549.1 + 420420	0.238	1224	−22.19	13	446	1023	246	253	22.6	35.8	0.05	1.56	1	1	3	4	219	237	29.8	37.9	0.05	1.55	3	4	3	4
RGZ J094443.2 + 024754	0.220[b]	1120	−23.49	37	447	1024	280	293	72.6	79.8	0.16	1.66	4	6	7	11	233	243	98.7	104.6	0.24	1.50	2	5	3	6
RGZ J095759.3 + 032725	0.165	814	−23.57	32	448	1025	169	176	256.2	259.9	0.41	0.97	4	9	9	15	134	142	292.8	295.3	0.29	0.96	4	9	7	14
RGZ J095759.3 + 191609	0.088[b]	413	−23.42	11	449	1026	98	98	122.7	125.9	0.17	1.36	6	13	11	23	65	66	149.6	153.1	0.26	0.96	6	9	16	22
RGZ J145001.5 + 144747	0.300	1593	−23.28	13	450	1027	87	89	28.1	29.9	0.28	1.48	0	3	0	3	80	84	32.0	34.1	0.34	1.17	2	2	2	2
RGZ J145039.8 + 441829	0.286	1508	−23.04	1	451	1028	320	328	84.4	90.5	0.14	1.20	3	4	5	8	255	264	110.6	114.1	0.36	1.03	2	5	5	10

Notes. [a]Continuum emission in RGZ J210030.5 + 100529 is hotspot dominated, and this source is excluded from analysis. [b]Only photometric redshift is available.
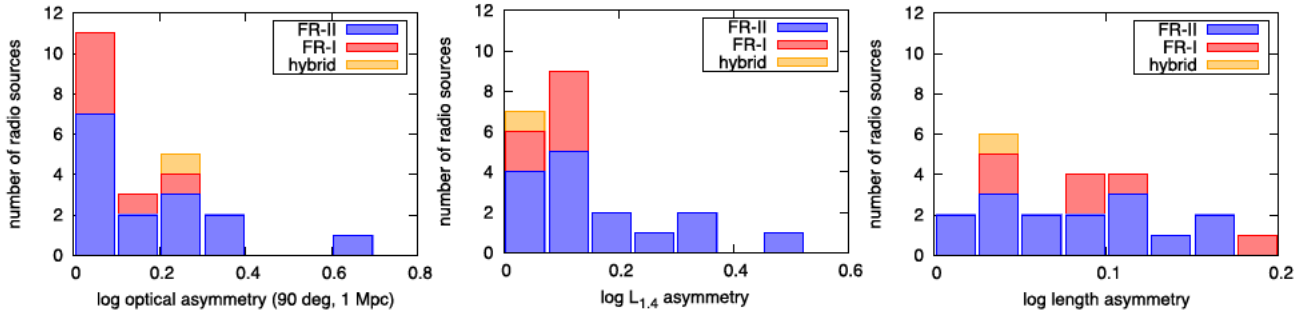
Figure 5. Distribution of asymmetries in radio source properties for FR-II (blue), FR-I (red), and hybrid (yellow) sources, shown as stacked bars. *Left*: Distribution of asymmetry in galaxy clustering associated with each lobe, defined as the decimal log of the ratio of the number counts of galaxies brighter than 20.5 mag in SDSS z-band, located within a 90 deg wedge of 1 Mpc radius centred on the host galaxy. *Middle*: Asymmetry in 1.4 GHz FIRST radio luminosity, integrated out to 5σ for each lobe. *Right*: Asymmetry in lobe lengths which are defined by the bounding rectangle described in Section 3.1 and Fig. 3.
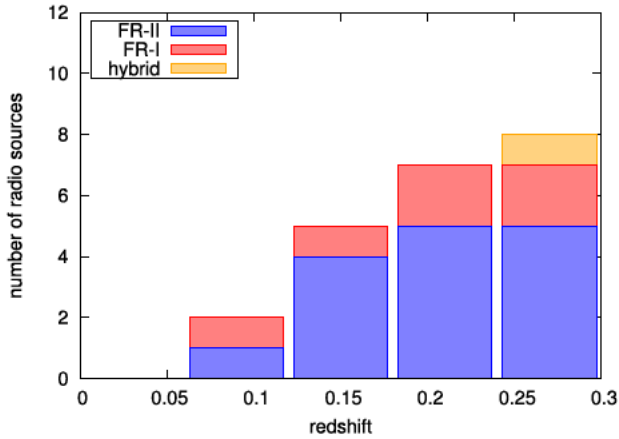

Figure 6. The distribution in redshift for sources out to the redshift limit $z = 0.3$, shown as stacked bars. Colours are as in Fig. 5.
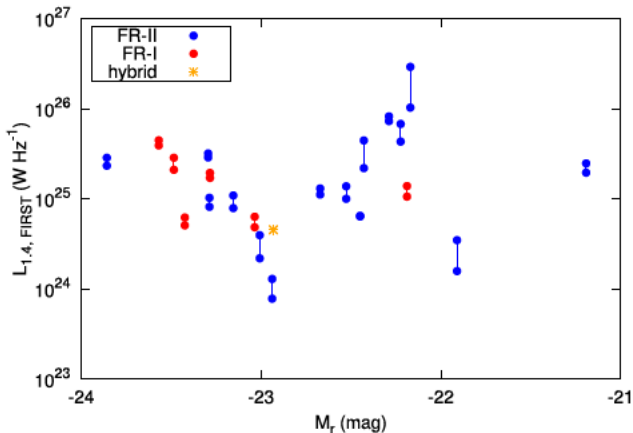

Figure 7. The host galaxy optical absolute r-band magnitude versus lobe luminosity for each source, known as the Ledlow–Owen relation, taken after Owen & Ledlow (1994). Each lobe is represented by a single point, with lobe pairs corresponding to a single source connected via a solid line. No clear separation of the classes is seen. Colours are as in Fig. 5.
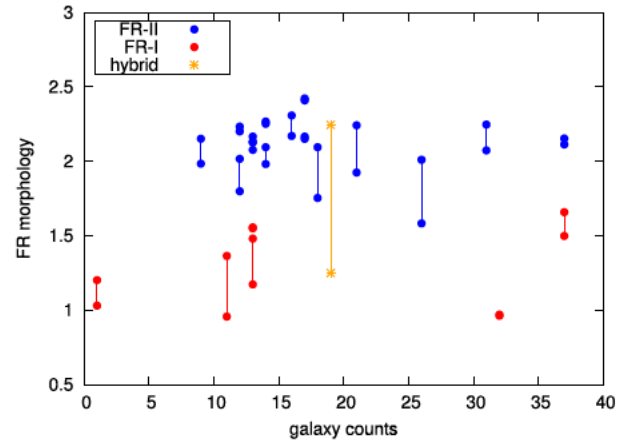

Figure 8. The FR index as a function of complete ($m_z > 20.5$ mag) SDSS galaxy counts within 1 Mpc of the active nucleus. Consideration of the large-scale environment does not provide a clear distinction between the morphologies in this sample. Colours are as in Fig. 5.

lobes, as described in Section 3.1, are used to estimate the direction of jet propagation are shown in Fig. 2 by the red line extending outwards from the host galaxy. We then define 'wedges' around each lobe, mirrored about the expansion axis and subtending angles of 45 and 90 deg; these are shown by dashed and solid grey lines

in Fig. 2. Neighbouring galaxies are assigned to a lobe if they are located within the appropriate wedge. By selecting for our sample only relatively straight pairs of lobes which are close to anti-parallel (to within approximately 10 deg), we ensure that all galaxies are associated with a maximum of only one lobe. The likelihood of including nearby isolated galaxies increases for lobes projected close to the line of sight; as sources with strong jet and hotspot emission have been excluded from this sample, projection effects will add further scatter but not cause any systematic effect.

Our sample consists of both nearby and more distant ($z = 0.3$) AGN. SDSS is 95 per cent complete at $m_z = 20.5$ mag, and we use this cut-off, converted to absolute magnitude, when calculating clustering associated with each lobe. This procedure allows us to compare environments of radio sources with different morphologies (Section 4). In Section 4.2, we consider the differences between two lobes of the same radio source. We quantify environment asymmetry by taking the ratio of total galaxy counts associated with each lobe, above the completeness limit (Fig. 4). This is broadly equivalent to taking the ratio of the normalization in the stellar mass function of galaxies associated with each lobe: we repeated the analysis below using estimates of the total stellar mass (summed over all galaxies) associated with each wedge (calculated using z-band magnitudes), and found similar results.
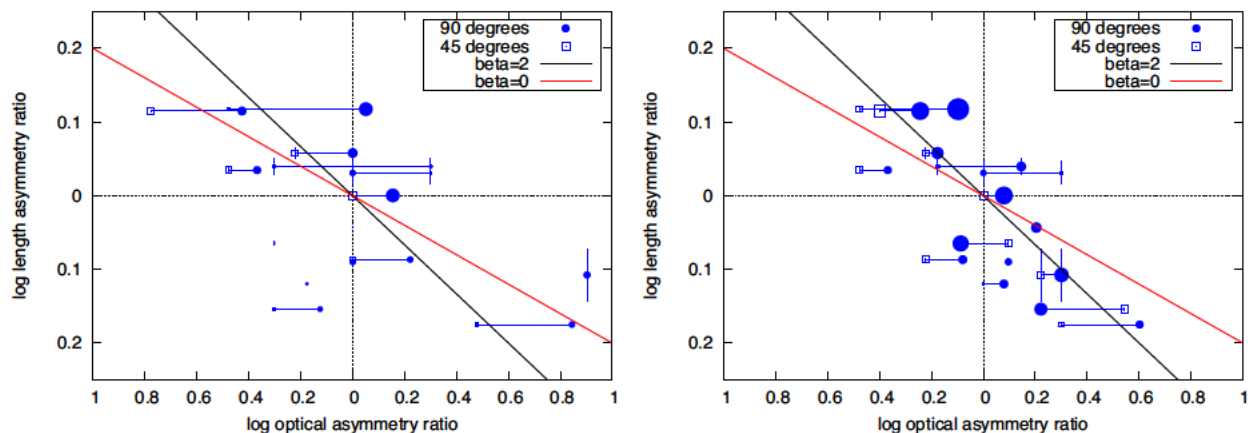
Figure 9. Asymmetry in FR-II lobe length and environment. Symbol size is proportional to the total number of galaxies used in the environment asymmetry calculation, i.e. larger points correspond to higher galaxy counts. Environment asymmetry is quantified using galaxies with photometric redshift consistent with the AGN host, within either 500 kpc (*left*) or 1 Mpc (*right*) from the host galaxy. Model predictions correspond to a flat ($\beta = 0$) density profile typical of inner ($\sim$30 kpc) regions of clusters; and steep ($\beta = 2$) environments more representative of large ($\gtrsim$100 kpc) clustercentric radii.
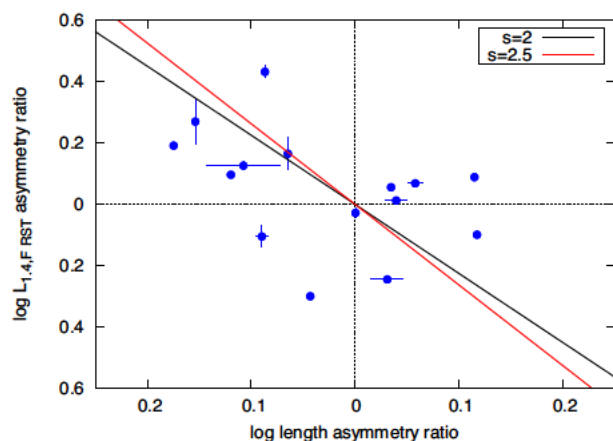

Figure 10. Lobe luminosity and length asymmetry for FR-II sources. Symbols are as in Fig. 9.

3.3 Sample statistics

The aim of this paper is to investigate the relationship between asymmetries in radio lobe and environment properties. The left-hand panel of Fig. 5 shows the distribution of optical asymmetries, quantified as the logarithm of the ratio of galaxy counts above the limiting z-band magnitude of 20.5 within 1 Mpc in a 90-deg wedge associated with each lobe. Asymmetries in excess of 0.6 dex (i.e. a factor of 4) are observed for FR-II sources. The middle panel of Fig. 5 shows a similar distribution for asymmetry in the radio continuum luminosity of each pair of lobes. Although FR-Is appear to show smaller asymmetries in both lobe continuum luminosity and galaxy counts, these differences are not statistically significant at the $p = 0.05$ level using the Wilcoxon–Mann–Whitney test. We note that although FR-Is are known to preferentially reside in more massive environments (Hill & Lilly 1991; Sabater et al. 2013) than FR-IIs, our selection bias against highly curved and asymmetric sources such as wide-angle tailed or head-tail radio galaxies will be an important contributing factor – for example, overdense environments may preferentially produce bent sources, as found in Garon et al. (submitted). The right-hand panel of Fig. 5 shows the distribution of length asymmetries for the sources in our

sample; again, we find no statistically significant difference at the $p = 0.05$ level between the FR-I and FR-II samples.

In Section 4.2, we investigate the relationship between radio and optical asymmetry diagnostics for the FR-II sources in our sample. We note again that length and luminosity measurements of FR-I sources are strongly affected by surface brightness sensitivity of observations (Shabala et al. 2017; Turner et al. 2018a) and should be interpreted with caution; we do not consider the FR-I sample in detail further in this work.

4 THE ROLE OF ENVIRONMENT

4.1 The relationship between radio source and host galaxy properties

The 16 FR-IIs and 6 FR-Is in our sample have similar redshift distributions (indistinguishable at the $p = 0.05$ level, shown in Fig. 6), and as such we can confidently compare the typical environments inhabited by the two morphological classes. Fig. 7, taken after Owen & Ledlow (1994), shows the relationship between lobe luminosity and host galaxy optical magnitude. We recover the previously found result that FR-Is are hosted by more massive galaxies (i.e. optically brighter) than FR-IIs, albeit at only at a 2σ confidence level, most likely due to the small FR-I sample size. There is however no clear separation between FR-I and FR-II sources in this plot, consistent with the results of Best (2009), who similarly used a redshift-matched sample.

Fig. 8 probes the large-scale environment (out to 1 Mpc) of the radio sources in our sample, quantified via counts of galaxies with $M_z < -20.47$ mag (corresponding to $m_z = 20.5$ mag at $z = 0.3$, our highest redshift). Perhaps surprisingly, FR-Is do not appear to inhabit denser environments as has been reported by several authors previously (e.g. Sabater et al. 2013; Miraghaei & Best 2017). This is again likely due to our selection effect against compact radio sources, which dominate number counts in dense environments (Shabala et al. 2008). Conversely, this result shows that the large-scale environment is not a crucial factor in the determination of the radio lobe morphology; the FR-I morphology is likely determined much closer to the active nucleus.
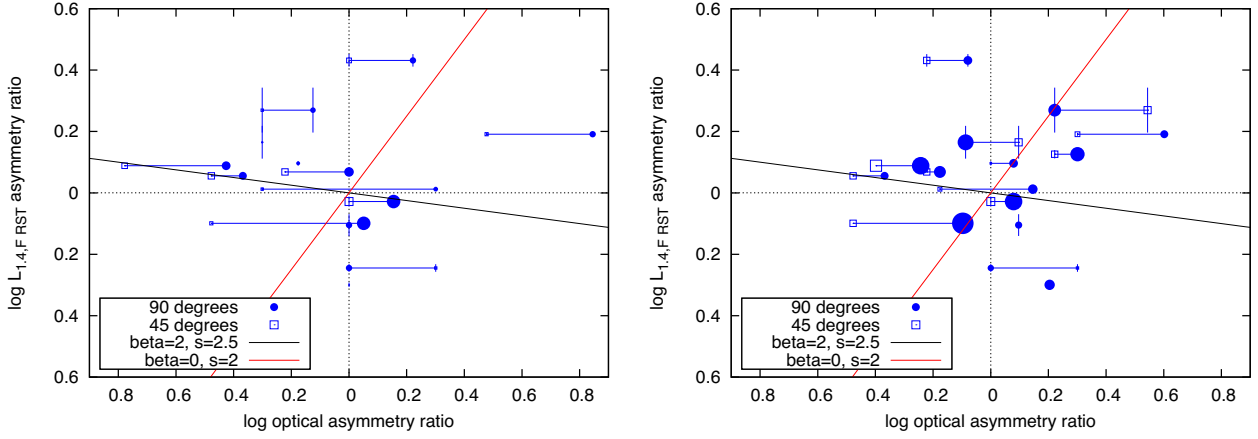
Figure 11. Asymmetry in FR-II lobe luminosity and environment. Panels and symbols are as in Fig. 9.

4.2 FR-II sources

4.2.1 Theoretical considerations

Dynamical models of double-lobed radio sources make clear predictions for the relationship between FR-II size, radio continuum luminosity, and environment properties. For a classical FR-II expanding into an atmosphere with a power-law density of the form $\rho(r) = \rho_0(r/r_0)^{-\beta}$, equations (1) and (4) of Shabala & Godfrey (2013) give the scalings between source linear size D, continuum luminosity L_ν and atmosphere gas density ρ_0 as,

$$D \propto \rho_0^{-\left(\frac{1}{5-\beta}\right)} \tag{1}$$

$$L_\nu \propto \rho_0^{\frac{5+s}{12}} D^{3-\left(\frac{4+\beta}{3}\right)\left(\frac{5+s}{4}\right)}, \tag{2}$$

where $s \approx 2 - 2.5$ is the power-law index of the electron energy distribution at the hotspot (Kaiser, Dennett-Thorpe & Alexander 1997; Willott et al. 1999; Turner, Shabala & Krause 2018b).

Assuming typical β values between 0 and 2, the expected scalings are

$$D \propto \rho_0^{[-0.33, -0.2]} \tag{3}$$

$$L_\nu \propto D^{[-2.63, -2.25]} \propto \rho_0^{[-0.13, +1.25]}. \tag{4}$$

The luminosity calculation above assumes no electron ageing, and a direct mapping between radio lobe pressure and continuum luminosity. In practice, factors such as spectral ageing (Murgia 2003; Turner 2018), non-equipartition magnetic fields (Croston & Hardcastle 2014), magnetic field inhomogeneities (Hardcastle 2013) and particle re-acceleration (Jones, Ryu & Engel 1999) will introduce significant scatter in the luminosity relations, and we therefore expect the size–density relation to be the tightest.

4.2.2 Dependence on the large-scale environment

Fig. 9 shows the relationship between lobe length asymmetry and galaxy clustering. Both quantities are calculated by taking the ratio of the relevant quantity (length, or galaxy counts above the completeness limit) of the eastern lobe divided by the western lobe. Environment asymmetry is calculated for both 500 kpc and 1 Mpc radii from the AGN host, and using galaxies within 45 and 90 deg

wedges centred on the lobe axis. Uncertainty in lobe length ratio is estimated by calculation of this quantity for two cuts in the signal-to-noise ratio, at 5σ and 3σ, respectively; length measurements of prominent FR-II lobes are not expected to vary substantially with the adopted noise cut. Regardless of the environment metric, there is a consistent, clear anti-correlation between these two quantities as indicated by a deficit of sources in the top right and bottom left corners of the plot. Moreover, the slope of the observed relation ($D \propto \rho_0^{-0.29\pm0.07}$, a non-zero slope at the 4σ level for the 500 kpc, 90 deg case) is consistent with expectation from analytical models that the galaxy clustering traces the underlying gas density profile, shown as solid lines for steep (black) and flat (red) gas density profiles. The best-fitting relationship suggests the typical radio source in the sample expands into a host environment with a pressure profile falling off with radius as $\rho_0 \propto r^{-1.6}$, representative of gas distribution at large cluster-centric radii.

The simplest analytical models of the kind described in Section 4.2.1 assume that radio lobes evolve self-similarly over their lifetime. This assumption is inconsistent with the observed increase in the radio source aspect ratio with length (Hardcastle et al. 1998; Turner et al. 2018b), which is also predicted by more realistic analytical models (Turner & Shabala 2015) and numerical simulations (Hardcastle & Krause 2013). Recent numerical simulation work (Vandorou et al., in preparation) shows that relaxing the self-similarity assumption can explain much of the observed scatter in the length–environment asymmetry relation shown in Fig. 9.

Fig. 10 shows the observed relationship between asymmetry in lobe length and luminosity. Definition of which emission belongs to the lobe is important: taking a higher threshold in the signal-to-noise ratio will systematically affect the lobe luminosity ratio by preferentially resolving out emission from the lower surface brightness lobe. Following our approach for lobe length measurement, the uncertainty in lobe luminosity ratio is again calculated by considering the difference in this quantity for signal-to-noise ratios of 3 and 5σ. Both the approximate anti-correlation of $L_\nu \propto D^{-3.9\pm1.9}$ (non-zero slope at the 2σ level) and large scatter in Fig. 10 are qualitatively consistent with the expectation from models. Idealized model predictions in Fig. 10 are only indicative as they do not take into account electron ageing, which will be significant for the large (and hence old) radio galaxies in our sample. The complex luminosity evolution of individual radio sources (by over an order of magnitude, and strongly environment dependent; Hardcastle & Krause 2013) will significantly contribute to the scatter in these

relations; for example, using FR-II samples carefully matched in jet power and source size, Shabala & Godfrey (2013) showed that environment can contribute approximately 0.3 dex to scatter in radio luminosity. We defer a detailed discussion of these points to future work.

Finally, we plot the relationship between lobe luminosity asymmetry ratio and environment in Fig. 11. Unlike lobe length, which increases monotonically with age, lobe luminosity is predicted to vary non-monotonically over the lifetime of a radio source; hence the lobe luminosity asymmetry ratio will depend on source age in addition to jet and environment properties (Hardcastle & Krause 2013; Shabala 2018). The lack of any correlation at above the 2σ level in Fig. 11 is expected from the wide range of factors which influence the lobe luminosity, as demonstrated by the broad range of predictions from analytical models (solid lines).

4.3 FR-I and hybrid sources

There are only six FR-I sources in our sample, hence we are unable to perform a similar analysis for these objects. From Table 1 there appears to be no obvious relationship between length or luminosity asymmetry and environment for FR-I sources, in broad agreement with complex expectations from the models. Jets are theoretically expected to propagate slower in denser environments (Kaiser & Alexander 1997); however, such environments may also be more conducive to keeping the jets collimated (Krause et al. 2012), allowing them to propagate further. Environmental boosting (Arnaud et al. 2010) is also likely to increase the jet surface brightness (and luminosity), enabling those jets propagating into denser gas to be visible to larger distances from the host galaxy (Shabala et al. 2017; Turner et al. 2018a). Given these competing effects and the small size of our sample, we are unable to draw any meaningful conclusions about the FR-I population.

A single hybrid radio source (RGZ J082835.2 + 322825) is present in our sample, and is shown in Fig. 2. The SW lobe shows a clear FR-II morphology, while the northern lobe appears to have a bright flare point followed by a gradual decrease in surface brightness. The FR indices are 2.24 and 1.25, respectively, consistent with the visual classification of this source as a hybrid. Small number statistics make environmental analysis difficult: there are four galaxies in a 90-deg wedge within 1 Mpc of the AGN host on the FR-I side, and seven galaxies on the FR-II side, reducing to only two galaxies on each side for a 45-deg wedge; we refrain from speculating on the causes of this source's morphology.

5 CONCLUSIONS

We have presented a sample of extended radio AGN identified as part of the RGZ citizen science project. Our sample consists of 16 FR-II objects, 6 FR-Is, and 1 hybrid morphology radio source. The environments into which these objects expand have been quantified using optical photometry from SDSS, to investigate the effect that the large-scale environment has on the size and luminosity evolution of radio sources. Small sample numbers preclude us from drawing any meaningful conclusions about the FR-I and hybrid populations.

For the FR-II sources, we find that

(i) The length of an FR-II radio lobe is strongly negatively correlated (statistically significant at the 4σ level) with the number density of galaxies in the environment into which it expands; this relationship is consistent with analytical models (e.g. Kaiser & Alexander 1997; Turner & Shabala 2015).

(ii) Luminosity ratio of FR-II lobes is moderately (statistically significant at the 2σ level) negatively correlated with the lobe length ratio, again consistent with analytical models.

(iii) There is no clear correlation between the asymmetry in luminosity of FR-II lobes and the number density of galaxies in their vicinity; the large observed scatter is consistent with the sensitivity of this relation to changes in the environment density profile and lobe electron energy distribution.

The excellent agreement between data and predictions from analytical models suggests that galaxy clustering provides a useful measure of the radio lobe environment. In the coming years, a combination of radio source models (e.g. Turner & Shabala 2015; Hardcastle 2018) and large-area radio continuum surveys supplemented by galaxy clustering information, such as the GAMA Legacy ATCA Southern Survey (GLASS), the Evolutionary Map of the Universe (EMU; Norris et al. 2011), and the LoFAR Two-metre Sky Survey (LoTSS; Shimwell et al. 2016), will enable a detailed census of the physical properties of radio AGN populations.

REFERENCES

Ahn C. P. et al., 2014, ApJS, 211, 17

Alexander P., 2006, MNRAS, 368, 1404

Arnaud M., Pratt G. W., Piffaretti R., Böhringer H., Croston J. H., Pointe-couteau E., 2010, A&A, 517, A92

Banfield J. K. et al., 2015, MNRAS, 453, 2326

Beck R., Dobos L., Budavári T., Szalay A. S., Csabai I., 2016, MNRAS, 460, 1371

Becker R. H., White R. L., Helfand D. J., 1995, ApJ, 450, 559

Best P. N., 2009, Astron. Nachr., 330, 184

Best P. N., Heckman T. M., 2012, MNRAS, 421, 1569

Best P. N., Kauffmann G., Heckman T. M., Brinchmann J., Charlot S., Ivezić Ž., White S. D. M., 2005, MNRAS, 362, 25

Best P. N., von der Linden A., Kauffmann G., Heckman T. M., Kaiser C. R., 2007, MNRAS, 379, 894

Bicknell G. V., 1995, ApJS, 101, 29

Blundell K. M., Rawlings S., 2000, AJ, 119, 1111

Bower R. G., Benson A. J., Malbon R., Helly J. C., Frenk C. S., Baugh C. M., Cole S., Lacey C. G., 2006, MNRAS, 370, 645

Burns J. O., 1990, AJ, 99, 14

Chon G., Böhringer H., Krause M., Trümper J., 2012, A&A, 545, L3

Churazov E., Brüggen M., Kaiser C. R., Böhringer H., Forman W., 2001, ApJ, 554, 261

Croston J. H., Hardcastle M. J., 2014, MNRAS, 438, 3310

Croton D. J. et al., 2006, MNRAS, 365, 11

Ellison S. L., Patton D. R., Hickox R. C., 2015, MNRAS, 451, L35

Fabian A. C., 2012, ARA&A, 50, 455

Fanaroff B. L., Riley J. M., 1974, MNRAS, 167, 31P

Gaspari M., Brighenti F., Temi P., 2015, A&A, 579, A62

Gawroński M. P., Marecki A., Kunert-Bajraszewska M., Kus A. J., 2006, A&A, 447, 63

Godfrey L. E. H., Shabala S. S., 2013, ApJ, 767, 12

Gopal-Krishna Wiita P. J., 2000, A&A, 363, 507

Hardcastle M. J., 2013, MNRAS, 433, 3364

Hardcastle M. J., 2018, MNRAS, 475, 2768

Hardcastle M. J., Krause M. G. H., 2013, MNRAS, 430, 174

Hardcastle M. J., Krause M. G. H., 2014, MNRAS, 443, 1482

Hardcastle M. J., Alexander P., Pooley G. G., Riley J. M., 1998, MNRAS, 296, 445

Hardcastle M. J., Evans D. A., Croston J. H., 2007, MNRAS, 376, 1849

Heesen V. et al., 2018, MNRAS, 474, 5049

Hill G. J., Lilly S. J., 1991, ApJ, 367, 1

Hodges-Kluck E. J., Reynolds C. S., 2011, ApJ, 733, 58

Jones T. W., Ryu D., Engel A., 1999, ApJ, 512, 105

Kaiser C. R., Alexander P., 1997, MNRAS, 286, 215

Kaiser C. R., Dennett-Thorpe J., Alexander P., 1997, MNRAS, 292, 723

Kapińska A. D. et al., 2017, AJ, 154, 253

Kaviraj S. et al., 2012, MNRAS, 423, 49

Komissarov S. S., 1994, MNRAS, 269, 394

Krause M., Alexander P., Riley J., Hopton D., 2012, MNRAS, 427, 3196

Lonsdale C. J. et al., 2003, PASP, 115, 897

Massaglia S., Bodo G., Rossi P., Capetti S., Mignone A., 2016, A&A, 596, A12

Middelberg E. et al., 2008, AJ, 135, 1276

Miraghaei H., Best P. N., 2017, MNRAS, 466, 4346

Mittal R., Hudson D. S., Reiprich T. H., Clarke T., 2009, A&A, 501, 835

Murgia M., 2003, Publ. Astron. Soc. Aust., 20, 19

Norris R. P. et al., 2006, AJ, 132, 2409

Norris R. P. et al., 2011, Publ. Astron. Soc. Aust., 28, 215

Owen F. N., Ledlow M. J., 1994, in Bicknell G. V., Dopita M. A., Quinn P. J., eds, ASP Conf. Ser. Vol. 54, The Physics of Active Galaxies. Astron. Soc. Pac., San Francisco. p. 319

Perucho M., Martí J. M., Laing R. A., Hardee P. E., 2014, MNRAS, 441, 1488

Planck Collaboration XVI, 2014, A&A, 571, A16

Pope E. C. D., Mendel J. T., Shabala S. S., 2012, MNRAS, 419, 50

Raouf M., Shabala S. S., Croton D. J., Khosroshahi H. G., Bernyk M., 2017, MNRAS, 471, 658

Rawlings S., Jarvis M. J., 2004, MNRAS, 355, L9

Sabater J., Best P. N., Argudo-Fernández M., 2013, MNRAS, 430, 638

Sadler E. M., Jenkins C. R., Kotanyi C. G., 1989, MNRAS, 240, 591

Shabala S. S., 2018, MNRAS, 478, 5074

Shabala S., Alexander P., 2009, ApJ, 699, 525

Shabala S. S., Godfrey L. E. H., 2013, ApJ, 769, 129

Shabala S. S., Ash S., Alexander P., Riley J. M., 2008, MNRAS, 388, 625

Shabala S. S., Kaviraj S., Silk J., 2011, MNRAS, 413, 2815

Shabala S. S., Santoso J. S., Godfrey L. E. H., 2012, ApJ, 756, 161

Shabala S. S., Deller A., Kaviraj S., Middelberg E., Turner R. J., Ting Y. S., Allison J. R., Davis T. A., 2017, MNRAS, 464, 4706

Shimwell T. W. et al., 2016, MNRAS, 459, 277

Silk J., Rees M. J., 1998, A&A, 331, L1

Tadhunter C., Dicken D., Morganti R., Konyves V., Ysard N., Nesvadba N., Ramos Almeida C., 2014, MNRAS, 445, L51

Turner R. J., 2018, MNRAS, 476, 2522

Turner R. J., Shabala S. S., 2015, ApJ, 806, 59

Turner R. J., Rogers J. G., Shabala S. S., Krause M. G. H., 2018a, MNRAS, 473, 4179

Turner R. J., Shabala S. S., Krause M. G. H., 2018b, MNRAS, 474, 3361

Willott C. J., Rawlings S., Blundell K. M., Lacy M., 1999, MNRAS, 309, 1017

Wright E. L. et al., 2010, AJ, 140, 1868
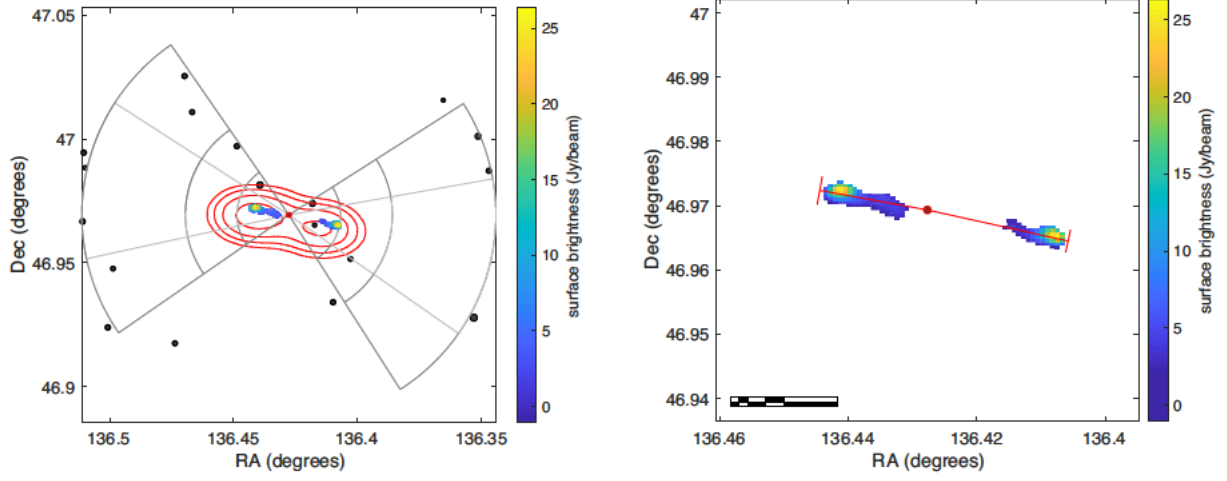
APPENDIX A: FR-II RADIO AND OPTICAL IMAGES

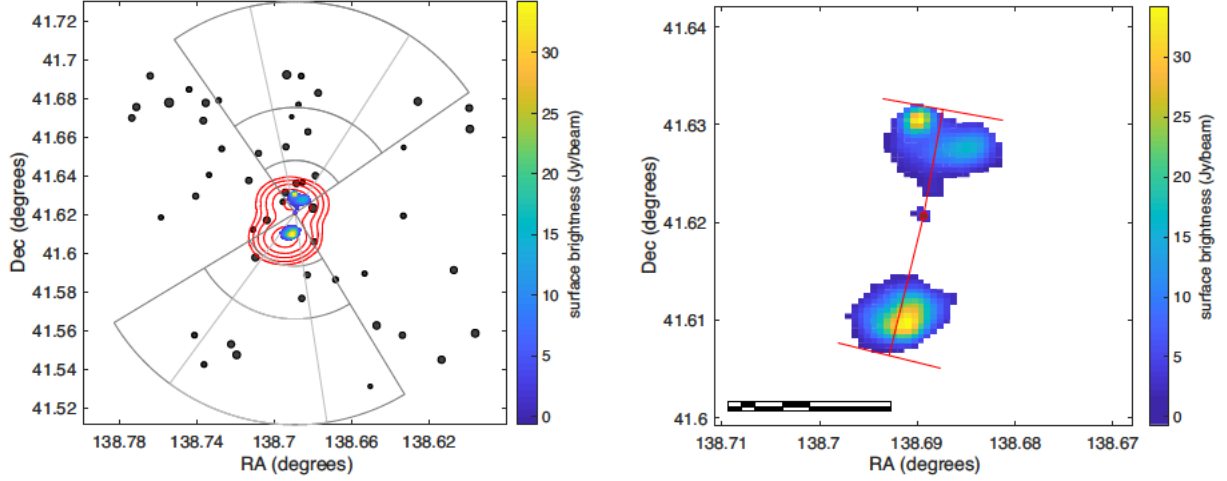**Figure A1.** FR-II source RGZ J090542.6 + 465809; symbols are as in Fig. 1.

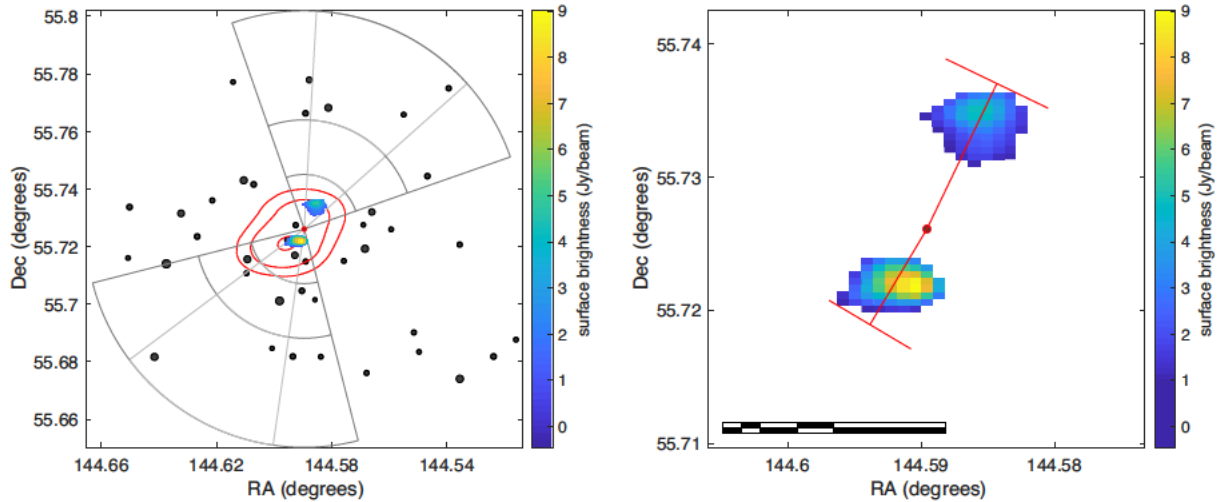**Figure A2.** FR-II source RGZ J091445.5 + 413714; symbols are as in Fig. 1.

Figure A3. FR-II source RGZ J093821.5 + 554333; symbols are as in Fig. 1.
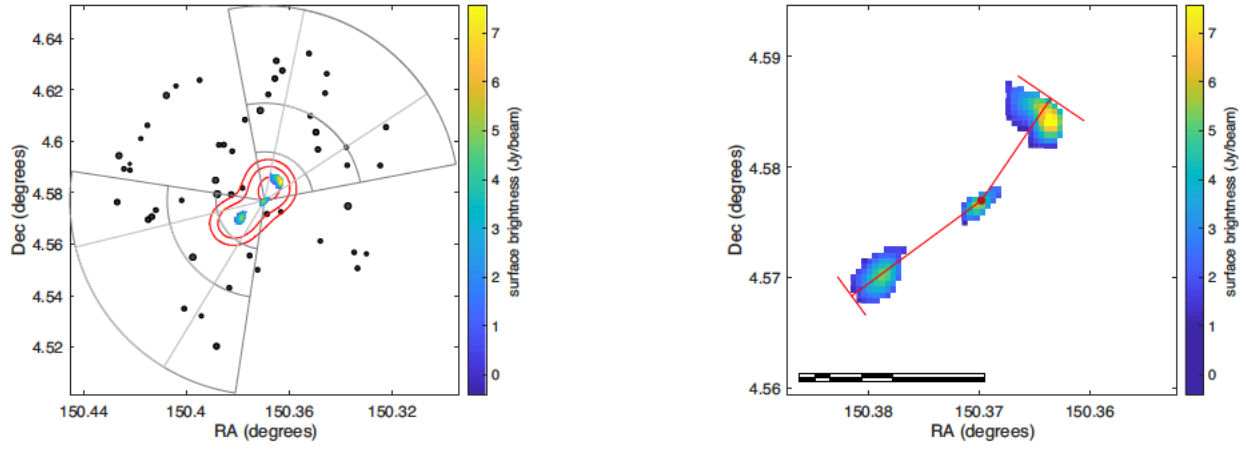
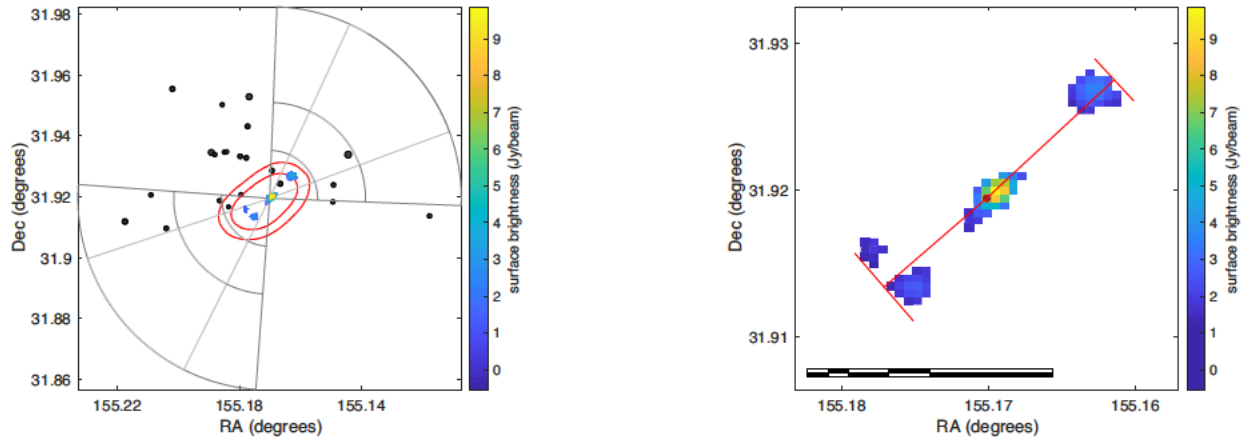**Figure A4.** FR-II source RGZ J100128.8 + 043437; symbols are as in Fig. 1.

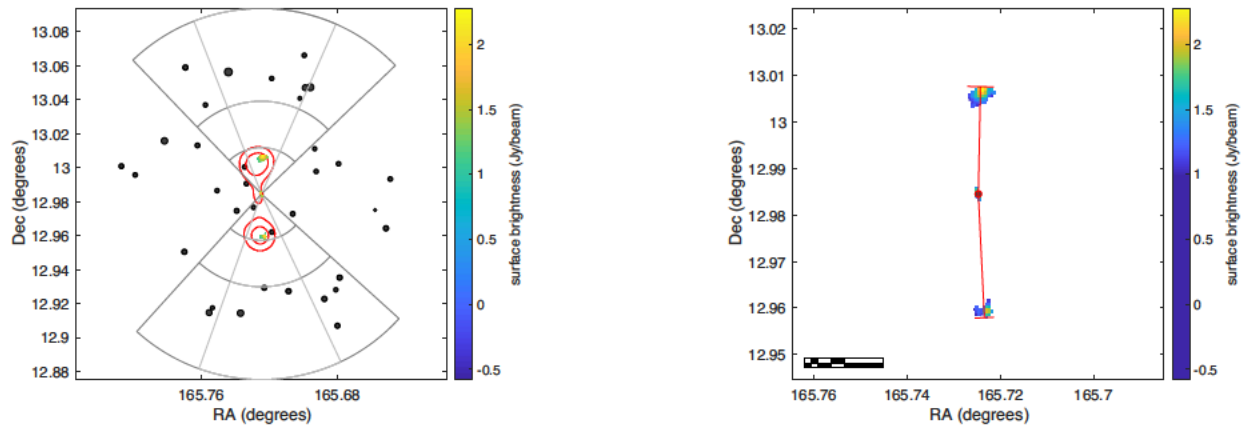**Figure A5.** FR-II source RGZ J102040.8 + 315509; symbols are as in Fig. 1.

Figure A6. FR-II source RGZ J110253.0 + 125904; symbols are as in Fig. 1.
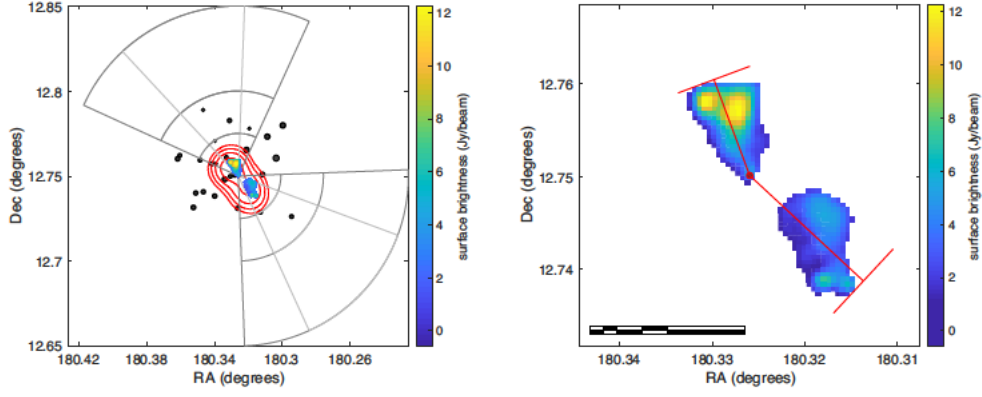
**Figure A7.** FR-II source RGZ J120118.2 + 124500; symbols are as in Fig. 1.
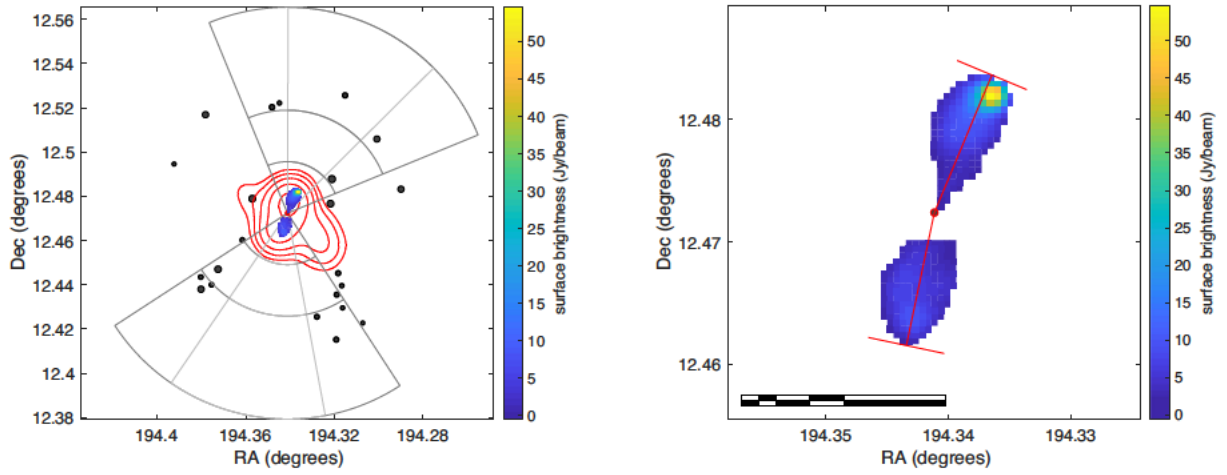
Figure A8. FR-II source RGZ J125721.9 + 122820; symbols are as in Fig. 1.
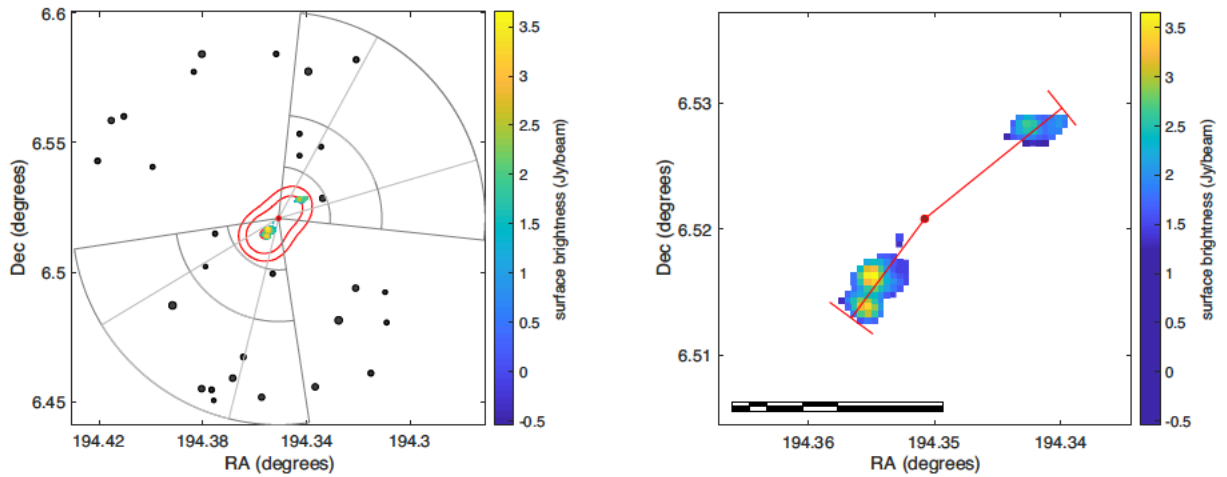
Figure A9. FR-II source RGZ J125724.2 + 063114; symbols are as in Fig. 1.
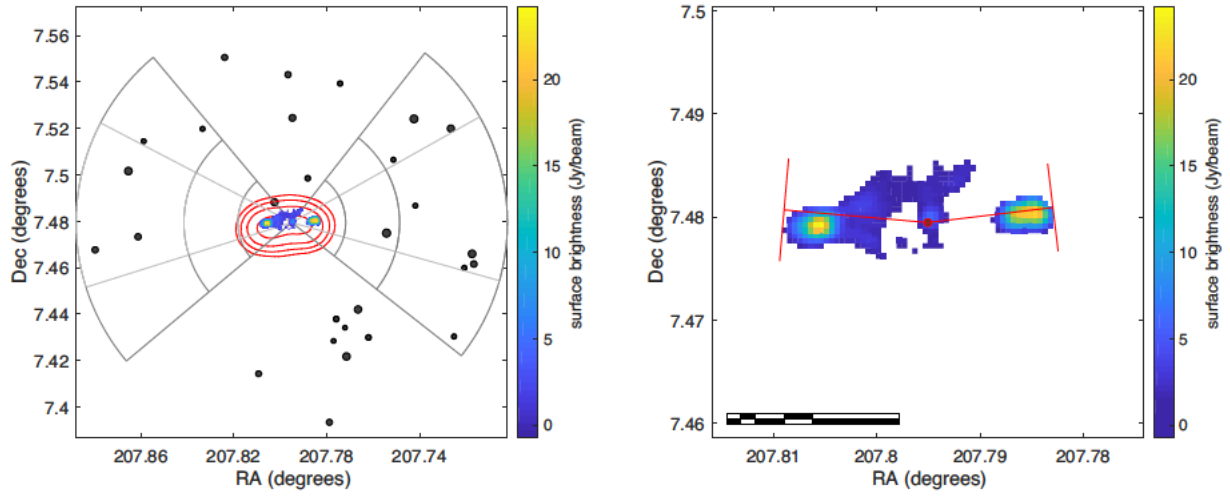
Figure A10. FR-II source RGZ J135110.8 + 072846; symbols are as in Fig. 1.
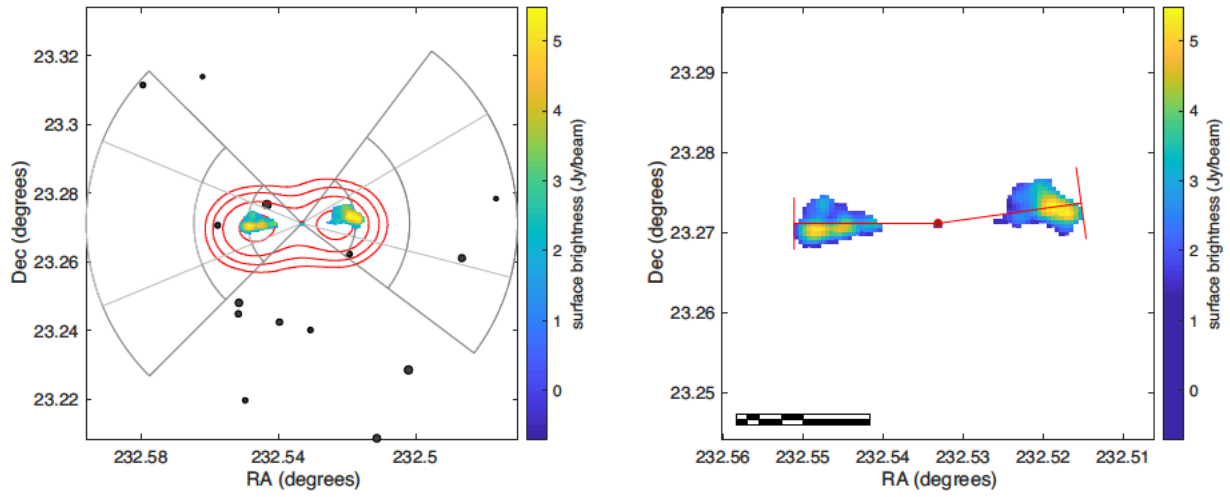
Figure A11. FR-II source RGZ J153008.0 + 231616; symbols are as in Fig. 1.
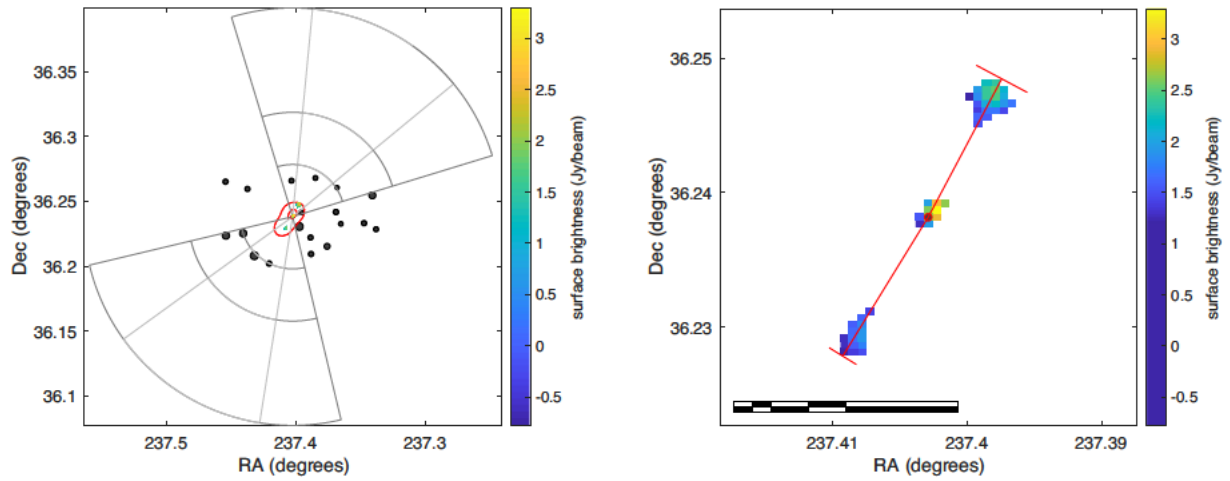
Figure A12. FR-II source RGZ J154936.7 + 361417; symbols are as in Fig. 1.
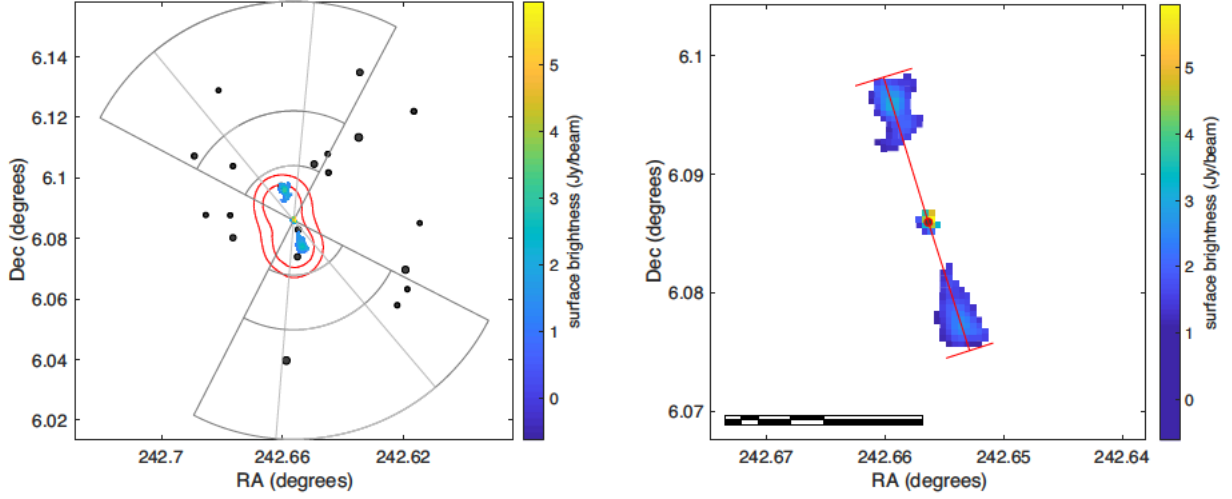
Figure A13. FR-II source RGZ J161037.5 + 060509; symbols are as in Fig. 1.
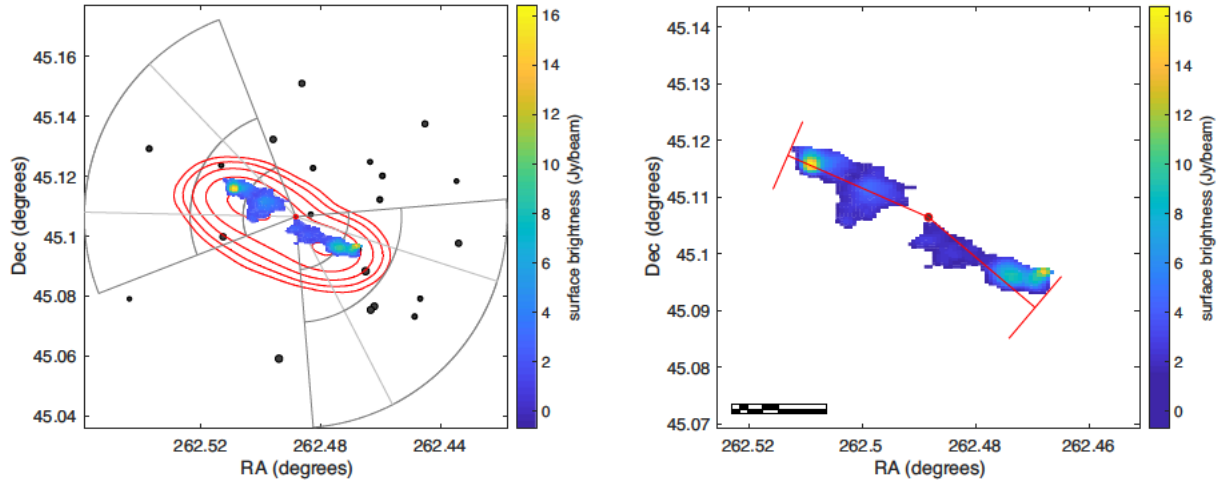
Figure A14. FR-II source RGZ J172957.2 + 450623; symbols are as in Fig. 1.
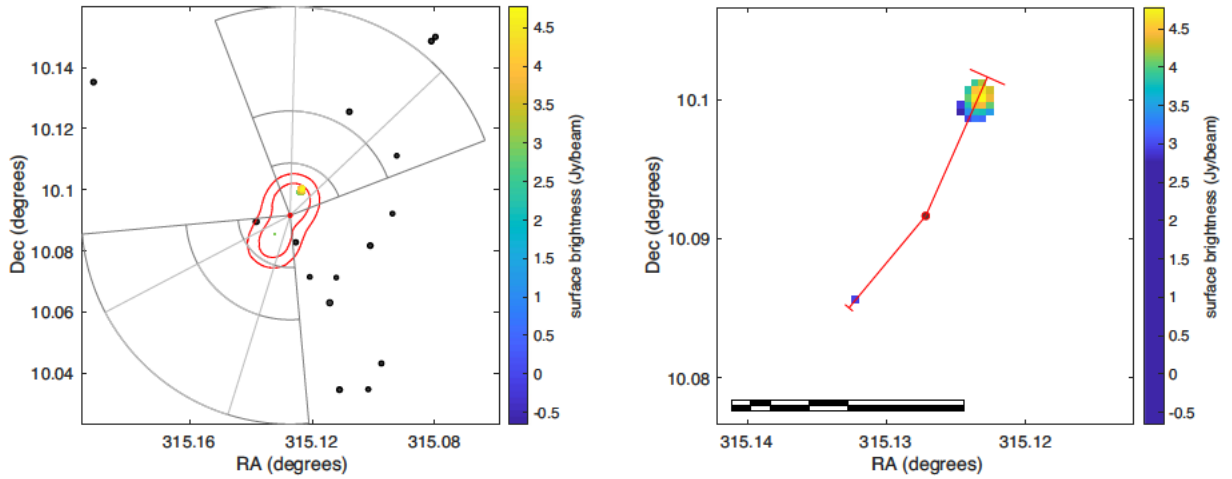
Figure A15. FR-II source RGZ J210030.5 + 100529; symbols are as in Fig. 1. This is the only FR-II source excluded from analysis, due to its hotspot dominance of integrated lobe luminosity.

APPENDIX B: FR-I RADIO AND OPTICAL IMAGES
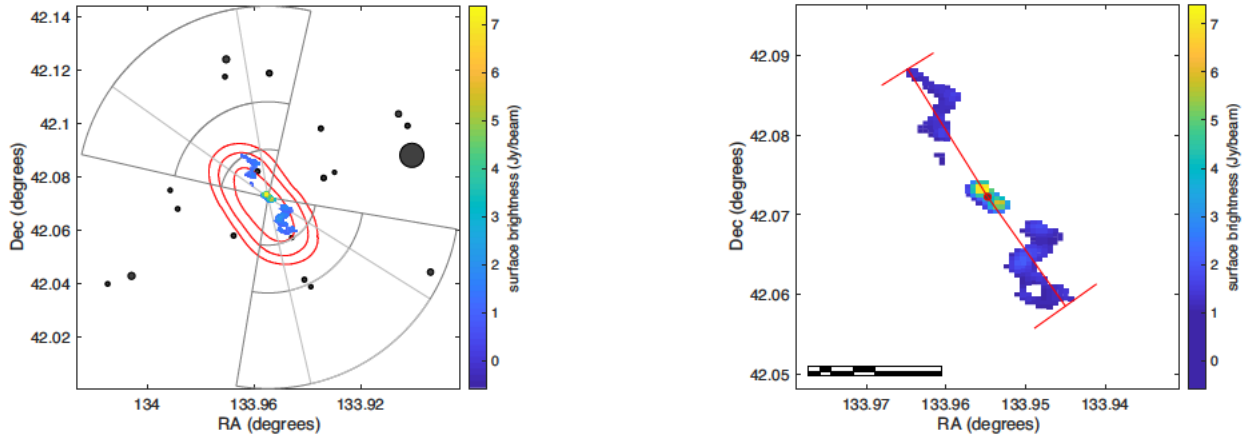
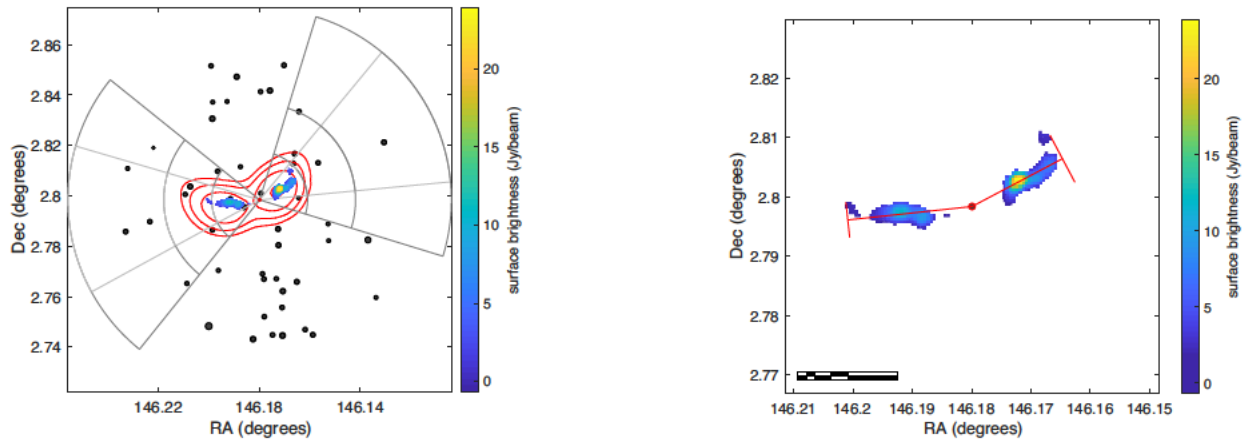
Figure B1. FR-I source RGZ J085549.1 + 420420; symbols are as in Fig. 1.

Figure B2. FR-I source RGZ J094443.2 + 024754; symbols are as in Fig. 1.
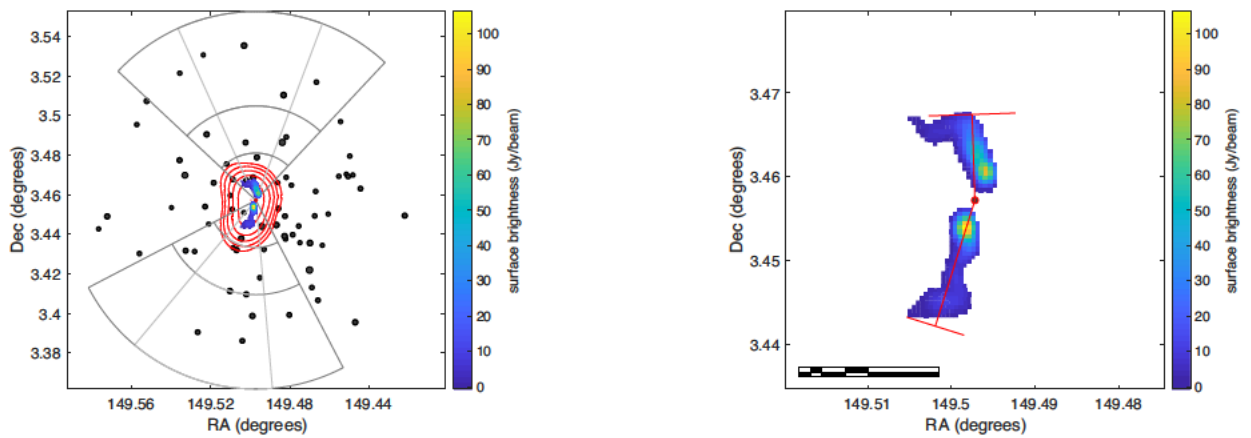

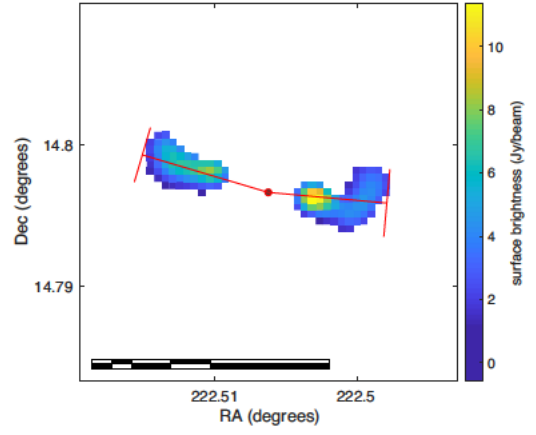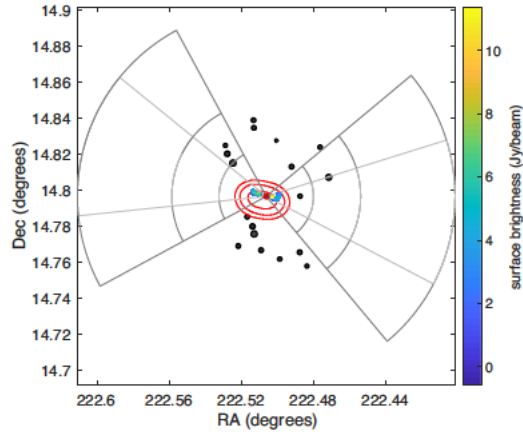**Figure B3.** FR-Isource RGZ J095759.3 + 032725; symbols are as in Fig. 1.

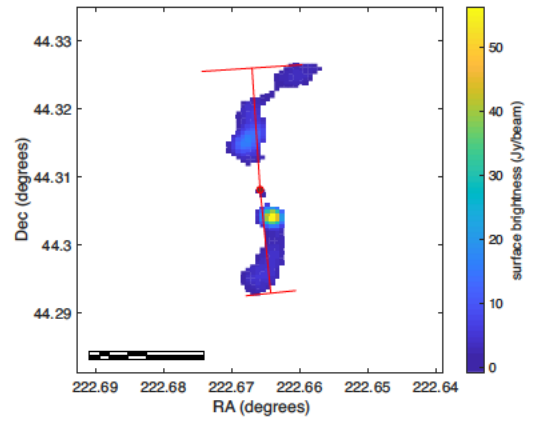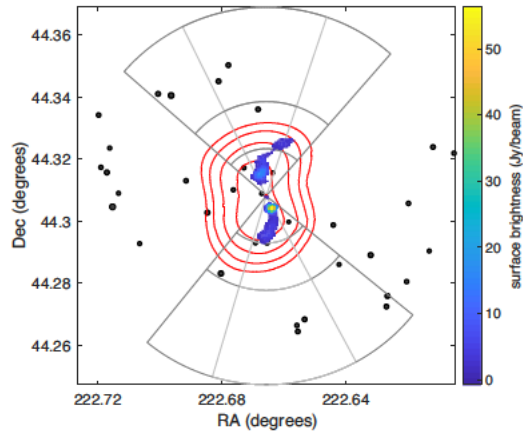**Figure B4.** FR-I source RGZ J145001.5 + 144747; symbols are as in Fig. 1.

Figure B5. FR-I source RGZ J145039.8 + 441829; symbols are as in Fig. 1.

This paper has been typeset from a TEX/LATEX file prepared by the author.